water

MDPI

Article

Degradation of Azo Dye Orange II Using BiOI/HKUST-1 Activated Persulfate under Visible Light Irradiation

Shumeng Zhang [1,2], Rui Wang [1], Xianxiong Cheng [1,*], Junfeng Lian [1,*], Xin Liu [1] and Jiahua Tang [1]

[1] Jiangxi Provincial Key Laboratory of Water Ecological Conservation at Headwater Regions, Jiangxi University of Science and Technology, 1958 Ke-Jia Road, Ganzhou 341000, China; zhangshumengme@126.com (S.Z.); liangzhang1029@163.com (R.W.); 15070760692@163.com (X.L.); gui56907@foxmail.com (J.T.)

[2] Hunan Research Institute for Nonferrous Metals Co., Ltd., 99 Yada Road, Changsha 410125, China

* Correspondence: chengxianxiong@163.com (X.C.); lianjf@jxust.edu.cn (J.L.); Tel.: +86-797-8312551 (X.C.); Fax: +86-797-8312088 (X.C.)

Abstract: Type I semiconductor heterojunction BiOI/HKUST-1 composites were prepared through a solvothermal method, with optimisation of the molar ratio and solvothermal reaction temperature. Comprehensive characterisation was conducted to assess the physical and chemical properties of the prepared materials. These composites were then evaluated for their ability to activate persulfate (PMS) and degrade high concentrations of azo dye orange II (AO7) under visible light conditions. The influence of various parameters, including catalyst dosage, PMS dosage, and initial AO7 concentration, were investigated. The AO7 degradation followed a pseudo-second order kinetic, and under visible light irradiation for 60 min, a degradation efficiency of 94.9% was achieved using a BiOI/HKUST-1 dosage of 0.2 g/L, a PMS concentration of 0.5 mmol/L, and an AO7 concentration of 200 mg/L. The degradation process involved a synergistic action of various active species, with O_2^-, $^1O_2$, and h^+ playing a pivotal role. Both BiOI and HKUST-1 could be excited by visible light, leading to the generation of photogenerated electron-hole pairs (e^--h^+); BiOI can efficiently scavenge the generated e^-, enhancing the separation rate of e^--h^+ and subsequently improving the degradation efficiency of AO7. These findings highlight the excellent photocatalytic properties of BiOI/HKUST-1, making it a promising candidate for catalysing PMS to enhance the degradation of azo dyes in environmental waters.

Keywords: bismuth iodide; metal-organic skeleton; heterojunction; persulfate; visible light catalysis

Citation: Zhang, S.; Wang, R.; Cheng, X.; Lian, J.; Liu, X.; Tang, J. Degradation of Azo Dye Orange II Using BiOI/HKUST-1 Activated Persulfate under Visible Light Irradiation. *Water* **2024**, *16*, 1805. https://doi.org/10.3390/w16131805

Academic Editor: Alexandre T. Paulino

Received: 6 May 2024
Revised: 17 June 2024
Accepted: 19 June 2024
Published: 26 June 2024

1. Introduction

Dyestuff is a common organic substance in textile, dyeing, and other industries. Dye wastewater is a huge hazard to humans and the environment and is difficult to biodegrade [1,2]. In recent years, advanced oxidation processes have been considered as one of the powerful technologies to overcome the shortcomings of conventional techniques for the treatment of dye wastewater [3]. Specifically, the breakage of -O-O- in the persulfate structure generates the strongly oxidising $\cdot SO_4^-$ ($E^0_{(\cdot SO4-)}$ = 3.10 V, $E^0_{(\cdot OH)}$ = 2.70 V) [4], which exhibits a stronger redox potential and a longer half-life compared to H_2O_2 [5,6] In the photocatalytic persulfate technology, the photocatalyst absorbs visible light energy to migrate the electron-hole pairs within it, which can react with the oxides in the system solution to form free radicals and directly with the pollutants. Moreover, free radicals and non-free radicals act simultaneously to degrade organic pollutants, which will significantly improve the efficiency of pollutant degradation. The establishment of a visible photocatalytic persulfate system to degrade dye wastewater is a green and effective means of addressing high-concentration wastewater treatment.

HKUST-1 is constructed from Cu^{2+} with the electron-providing organic ligand homophthalic tricarboxylic acid (BTC) [7] and exhibits an octahedral structure that can be synthesised under mild conditions. HKUST-1 has a tunable pore size and a specific surface

area, a highly ordered crystalline porous network [8], and excellent chemical stability [9]. Williams et al. (1999) first synthesised HKUST-1, which has received much attention in the fields of gas storage, catalysis, and photovoltaics [10]. However, the poor separation and transfer ability of photogenerated carriers makes HKUST-1 inefficient in photocatalytic processes [11]. In recent years, the construction of heterojunction photocatalysts by combining two or more photocatalysts with suitable energy band structures has become one of the effective methods to regulate the transfer path and separation of photogenerated carriers [12]. For example, Sheikhsamany et al. prepared $BaTi_{0.85}Zr_{0.15}O_3$/MOF-199 (HKUST-1) nanocomposites with a one-pot method, and the 30% composite material showed 90.24% degradation efficiency of tetracycline [13]. Wu et al. prepared NCFOH/HKUST composites for degradation of active orange 5 (RO5) by directly depositing and growing HKUST on nanoscale copper ferrite (NCFOH) [14]. RO5 degraded more than 98% in 80 min [14]. The new bismuth-based photocatalyst BiOI material is a p-type semiconductor with a band gap width of 1.8 eV [15], a unique graphite-like layered structure [16], and a good visible light response. However, BiOI alone still suffers from insufficient degradation efficiency strength and electron-hole pair compounding [17]. Photocatalysis can significantly improve the treatment efficiency and degradation rate of wastewater and has the characteristics of green and no secondary pollution in wastewater treatment, while higher light absorption in the visible range, higher carrier separation ability, and suitable band gap will be the desirable characteristics for sustainability. BiOI and HKUST-1 have matching band gap energies, and the formation of heterojunctions between them can overcome their own defects, enhancing stability and accelerating photogenerated electron-hole pair transfer. The modulation of the crystal structure and micromorphology of semiconductors is also a key influence in increasing the visible light absorption range and effective photogenerated carrier separation [18].

In this work, type I BiOI/HKUST-1 heterojunction photocatalysts were prepared from a solvothermal method and characterised by different tests for their morphological properties, crystal structures, specific surface areas, and chemical valence states. The morphological properties of the photocatalysts were optimised by adjusting the temperatures and molar ratios in a solvothermal method. At the same time, the photocatalysts were introduced into an advanced oxidation system to catalyse persulfate to efficiently degrade high-concentration dye wastewater. The degradation efficiency of six systems for AO7 and the effects of catalyst concentration, pollutant concentration, and persulfate (PMS) concentration on the degradation systems were investigated, and kinetic fitting was carried out. The optimal degradation parameters of AO7 were determined. The degradation mechanism in BiOI/HKUST-1 heterojunction visible photocatalytic peroxynitrite degradation of AO7 was investigated through free radical burst experiments and UV-visible spectrograms.

2. Materials and Methods

2.1. Major Reagents

Bismuth dinitrate pentahydrate ($Bi(NO_3)_3{\cdot}5H_2O$), potassium iodide (KI), ethylene glycol ($C_2H_6O_2$, EG), and acetic acid (CH_3COOH) were purchased from Sinopharm Chemical Reagent Co.,Ltd. (Shanghai, China), Potassium peroxymonosulfate ($KHSO_5$, 42~46%), L-Histidine ($C_6H_9N_3O_2$), and p-benzoquinone ($C_6H_4O_2$, BQ) were bought from Shanghai McLean Biochemical Technology Co. (Shanghai, China), Anhydrous ethanol (C_2H_6O, EtOH), sodium bicarbonate ($NaHCO_3$), sodium chloride (NaCl), sodium sulfate (Na_2SO_4), and tert-butanol ($C_4H_{10}O$, TBA) were purchased from Silong Science Co. (Shantou, China), Sodium carbonate (Na_2CO_3), orange II ($C_{16}H_{11}N_2NaO_4S$, AO7), and sodium nitrate ($NaNO_3$) were provided by Ron's Reagents Ltd. (Shanghai, China). All the above reagents are analytically pure.

2.2. Preparation of HKUST-1

Metal-organic skeleton material HKUST-1 was prepared with a solvothermal method. $Cu(NO_3)_2{\cdot}3H_2O$ (1.499 g) and BTC (0.84 g) were weighed to achieve $n(Cu^{2+})$:n(BTC) = 3:2.

The above solvents were dissolved in a mixed solution composed of 20 mL of H_2O, 20 mL of EtOH, and 20 mL of EG. After stirring for 30 min, the solution was fully mixed and transferred to a 100 mL PTFE-lined reaction kettle kept in a muffle furnace at 120 °C for 6 h. After the system was cooled to room temperature, it was washed three times with deionised water and anhydrous ethanol separately and dried in an oven at 60 °C for 12 h to obtain blue HKUST-1.

2.3. Preparation of BiOI/HKUST-1 Heterojunction

The BiOI/HKUST-1 photocatalytic composite was synthesised with a solvothermal method using ethylene glycol as a solvent. $Bi(NO_3)_3{\cdot}5H_2O$ (0.485 g) was dispersed into a mixed solution consisting of 20 mL of EG and 5 mL of acetic acid, noted as solution A. A certain mass of HKUST-1 (0.198, 0.329, 0.461, and 0.659 g) and 0.166 g of KI were dissolved in 25 mL of EG, stirred well, and recorded as solution B. Solution A was continuously dripped into solution B to form a green mixture. The mixed solution was transferred to a 100 mL PTFE-lined autoclave and reacted in a muffle furnace at different temperatures for 6 h before being allowed to cool naturally to room temperature. The solution was then washed three times with deionised water and anhydrous ethanol separately to remove residual chemicals. Finally, the composites were dried in an oven at 60 °C for 12 h to obtain the BiOI/HKUST-1 photocatalytic composite. Based on different molar ratios of BiOI to HKUST-1 [n(BiOI):n(HKUST-1) = 0.3, 0.5, 0.7, and 1.0] and different solvent heat temperatures (100, 120, and 160 °C), the products were named BH-0.3-120, BH-0.5-120, BH-0.7-120, BH-1.0-120, BH-0.7-100, and BH-0.7-160.

2.4. Degradation Experiments

A certain amount of a powdered catalyst was dispersed into 100 mL of a 200 mg/L AO7 solution. The reaction system was first darkened for 30 min at room temperature (25 °C) to reach adsorption–desorption equilibrium, and then a certain amount of PMS was added. The degradation reaction was carried out under irradiation with a 350 W xenon lamp ($\lambda \geq 420$ nm) for a total duration of 60 min. Water samples were taken at a 10 min interval and filtered through a 0.45 μm membrane. Then, 2 mL of ethanol was added to quench the residual free radicals and the AO7 concentration was measured with a UV-Vis spectrophotometer.

2.5. Analysis Methods

The characteristic peak of AO7 occurs at 484 nm and its concentration can be detected using a UV-Vis spectrophotometer. The AO7 degradation efficiency was calculated according to Equation (1). A pseudo-secondary kinetic model (Equation (2) was also used to fit the kinetics to the catalytic degradation system data and to visually reflect the differentiation in the degradation capacity of different systems for AO7.

$$\text{Degradation rate (\%)} = (C_0 - C)/C_0 \times 100\% \quad (1)$$

$$1/C - 1/C_0 = k_{obs}{\cdot}t \quad (2)$$

where C_0 and C are the pollutant concentrations initially and at a given moment, respectively, mg/L; k_{obs} is the pseudo-secondary kinetic constant, min^{-1}; and t is the reaction time, min.

3. Results and Discussion

3.1. Characterisation of the Catalysts

3.1.1. Scanning Electron Microscopy (SEM) and X-ray Energy Spectrometry (EDS)

The morphology of powdered BiOI, HKUST-1, and BH with different molar ratios and different solvent heat temperatures was observed under SEM (Figure 1a–h).

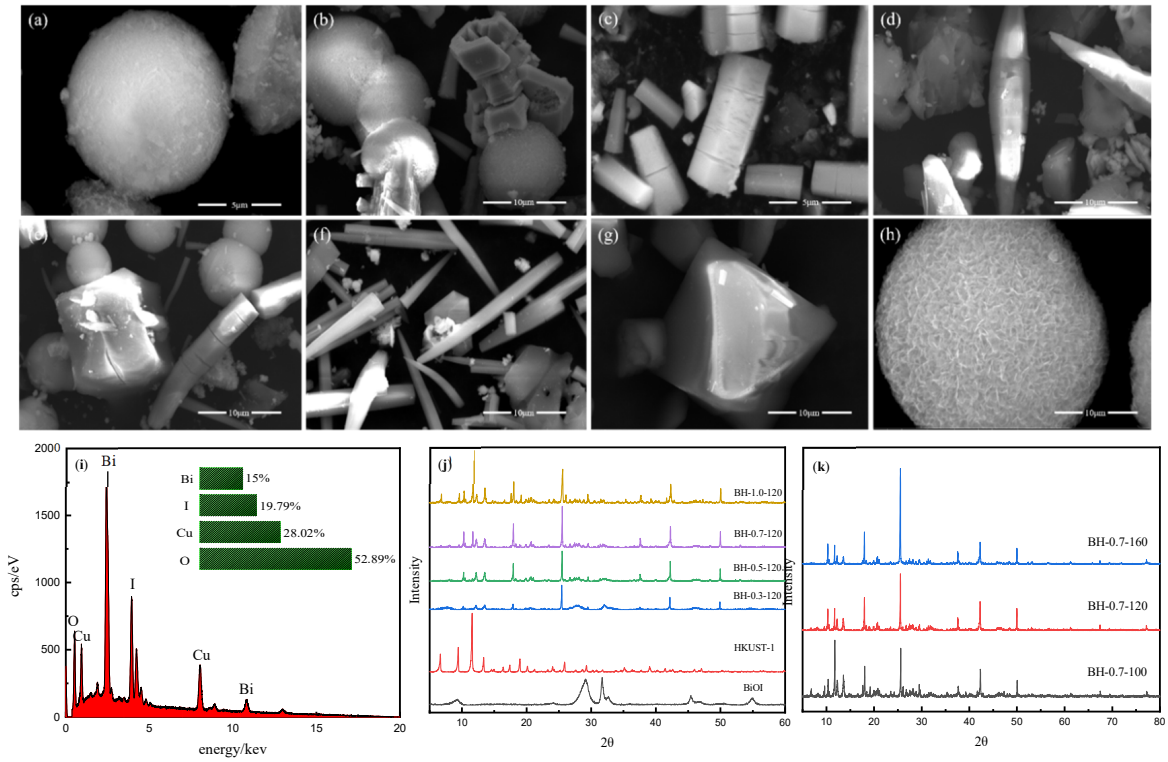

Figure 1. The SEM images of (**a**) BH-0.3-120, (**b**) BH-0.5-120, (**c**) BH-0.7-120, (**d**) BH-1.0-120, (**e**) BH-0.7-100, (**f**) BH-0.7-160, (**g**) HKUST-1, and (**h**) BiOI; the EDS images of BH-0.7-120 (**i**), XRD pattern of BH samples prepared at different molar ratios (**j**), and reaction temperatures (**k**).

The individual BiOI presents a regularly shaped 3D spherical structure with a surface composed of numerous light and thin nanosheets (Figure 1h). The pure HKUST-1 shown in Figure 1g is a positive octahedral structure with a smooth surface. As the ratio of n(BiOI):n(HKUST-1) increases, BH switches from a spherical to columnar structure, and the morphology of BH-0.3-120 shows a smooth, rounded spherical shape, at which point the BiOI takes up a larger proportion and shows a BiOI-like morphology. The morphology of BH-0.5-120 shows BiOI partially bound to HKUST-1. When the n(BiOI):n(HKUST-1) ratio reaches 0.7, BiOI is completely bound to HKUST-1, showing a broken columnar structure. The morphology of BH-1.0-120 shows a needle-like structure with two small ends and a large middle part. The solvent heat temperatures also affect the properties and morphology of the materials as-prepared. At a controlled reaction heat temperature of 100 °C, BH-0.7-100 shows three shapes (spherical, octahedral, and columnar), indicating that the lower temperature did not cause the crystallisation of the composite. The morphology of BH-0.7-120 is columnar and that of BH-0.7-160 is smooth and elongated needle-like. The BH-0.7-120 EDS plot in Figure 1i shows the characteristic peaks of Cu, O, I, and Bi, with no other impurity peaks, indicating that the BH-0.7-120 composite has been successfully bonded.

3.1.2. X-ray Diffraction (XRD)

XRD reveals the crystal structures of the materials prepared at different ratios and temperatures (Figure 1j,k).

The characteristic diffraction peaks of BiOI occur at 2θ = 9.658, 29.645, 31.657, 45.666, and 55.150° ascribed to the (001), (102), (110), (104), and (212) crystal planes, respectively. The main diffraction peaks of HKUST-1 occur at 2θ = 5.7, 9.5, 11.6, 13.5, 17.5, 25.9, and 29.3° and belong to the (200), (220), (222), (400), (511), (731), and (751) crystal planes, respectively. For the BiOI/HKUST-1 composite, all diffraction peaks belong to BiOI and HKUST-1 [19]. The characteristic peaks are sharp and flat, and no new peaks appear, indicating that the composites as-prepared are free from other impurities. As the molar ratio of BiOI/HKUST-1

rose, the characteristic peaks of HKUST-1 increased in intensity (2θ = 11.6, 17.5°) and the characteristic peaks of BiOI decreased in intensity (2θ = 29.65, 31.66°). As the reaction temperature of the BiOI/HKUST-1 composites rose, the peaks were sharper and flatter, indicating that the crystallisation of the products was more complete.

3.1.3. Ultraviolet-Visible Diffuse Reflectance Spectroscopy (UV-Vis)

Based on the results of UV-Vis diffuse reflectance spectroscopy, the light absorption capacity and the forbidden band width of HKUST-1 and its composites BH-0.3-120, BH-0.5-120, BH-0.7-120, BH-1.0-120, BH-0.7-100, and BH-0.7-160 were analysed. The forbidden band width (Eg) of all samples was deduced from Equations (3) and (4) proposed by Tauc et al. [20]:

$$h\nu = hc/\lambda = 1240/\lambda \quad (3)$$

$$\alpha h\nu = A(h\nu - Eg)^{1/n} \quad (4)$$

where α, h, v, λ, c, and A are the optical absorption coefficient, Planck's constant, optical frequency, wavelength (nm), wave speed, and absorbance, respectively, and the value of n depends on the mode of leap in the semiconductor (n = 1 for direct leap semiconductors, n = 1/2 for indirect leap semiconductors) [21].

As shown in Figure 2a–c, The absorption wavelength of HKUST-1 at 233–320 nm is due to the strong absorption of the BTC ligand of HKUST-1 in the near-UV region and the ligand metal charge transfer between the carboxylate and copper atoms [22]. The absorption edge of HKUST-1 is located at 478 nm due to the d-d jump in the Cu^{2+} centre [23], which has a low absorption utilisation of visible light. Compared to HKUST-1, all composites show a significant red shift in the absorption edge, enhancing the intensity of light absorption in 478–588 nm. The wider absorption edge of the BH-0.3-120 material compared to BH-0.5-120, BH-0.7-120, and BH-1.0-120 is due to the higher content of BiOI, which may correspond to the narrow band gap and large absorption range of BiOI. The forbidden band width of the material can be deduced from the tangent line in the curve of $(\alpha h\nu)^{1/2}$ versus hν, which is approximately 2.43 eV for HKUST-1 and 1.80 eV for BiOI according to previous studies. The band gaps of the composites all lie between the band gaps of the individual materials, suggesting that some interaction between the BiOI and HKUST-1 components and some mixing states between the interfaces occurred as well as the possible formation of heterojunctions, and that these mixing states altered the Eg of the composites [12]. The forbidden band widths of BH-0.3-120, BH-0.5-120, BH-0.7-120, and BH-1.0-120 are 2.09, 2.05, 2.19, and 2.22 eV, respectively. The narrowing of the forbidden band width of the composites demonstrates that BiOI alters the electronic properties of HKUST-1 and broadens the photoresponse range of photocatalysis. To further investigate the energy band positions of individual components in the heterojunction to study the photodegradation mechanism of the photocatalytic system, the conduction and valence band values of BiOI and HKUST-1 were calculated using Mulliken's electronegativity theory equations:

$$E_{VB} = \chi - Ee + 0.5E_g \quad (5)$$

$$E_{CB} = E_{VB} - E_g \quad (6)$$

where χ is the geometric mean of the electronegativity of the constituent atoms in the semiconductor, Ee is the energy of the free electron (~4.5 eV vs. NHE), E_{CB} is the conduction band potential energy of the catalyst, and E_{VB} is the valence band potential energy of the catalyst. Half the value of the sum of the first ionisation energy (Ei) and the electron affinity (Ea) of its constituent elements is used to estimate the electronegativity of each semiconductor [24]. The calculation results and related data are shown in Table 1. These data suggest that BiOI and HKSUT have suitable energy band potentials to construct heterojunction structures. A possible type I heterojunction charge transfer mechanism is proposed to elucidate the excellent photocatalytic performance of the binary BiOI/HKSUT-1 photocatalyst. The CB and VB edges of BiOI are wrapped by the energy gap of HKUST-1.

HKUST-1 shows the typical structural features of a type I heterojunction [25]. When the light energy ≥ the band gap energy of the catalyst, both BiOI and HKUST-1 will be excited by visible light, producing photogenerated electrons on the CB and photogenerated holes on the VB. Moreover, the accumulated photogenerated holes on the VB of BiOI and HKSUT-1 react with H_2O molecules and OH^-, since the VB potentials of BiOI (+2.34 eV vs. NHE) and HKUST-1 (+2.61 eV vs. NHE) are much higher than those required for ·OH formation (·OH/H_2O = +1.99eV vs. NHE, ·OH/OH^- = +2.40 eV vs. NHE), which is the same as the results of the radical trapping experiments.

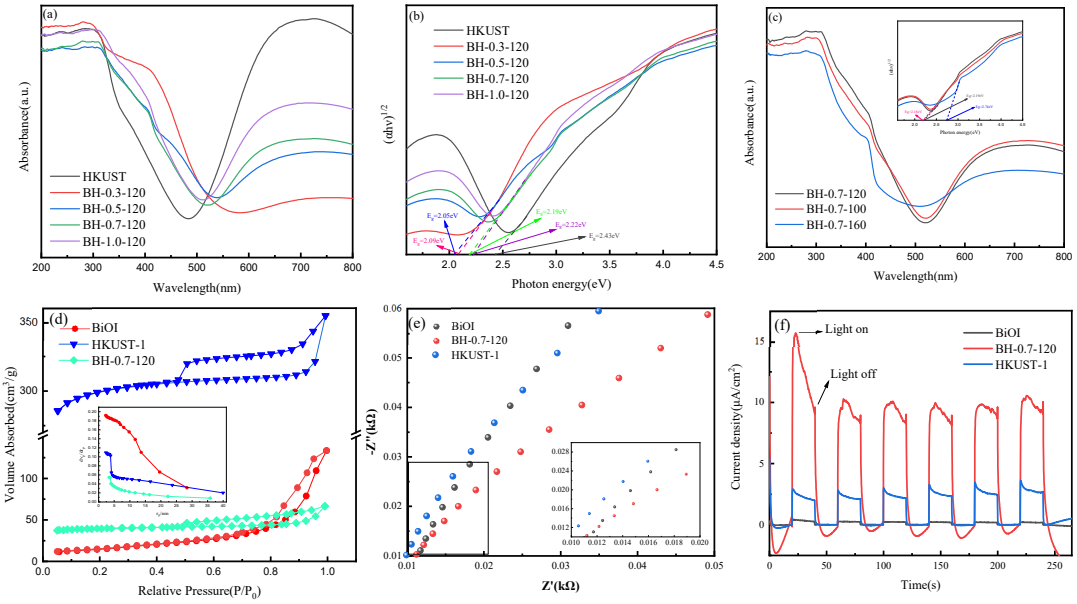

Figure 2. Ultraviolet-visible diffuse reflection spectra of BH samples at different molar ratios (**a**,**b**) and reaction temperatures (**c**); nitrogen adsorption–desorption isotherms with different catalysts (**d**); photocurrent response (**e**) and electrochemical impedance spectra (**f**) of different catalysts.

Table 1. Summary of E_{VB} and E_{CB} data for calculating composite composition.

Catalyst	χ	Eg	E_{VB}	E_{CB}
BiOI	5.94 eV [26]	1.8 eV	2.34 eV	0.54 eV
HKUST-1	5.89 eV [27]	2.43 eV	2.61 eV	0.18 eV
BH-0.7-120	-	2.19 eV	-	-

3.1.4. Brunauer, Emmett, and Teller (BET) Analysis

The specific surface area, pore volume, and pore size distribution of BiOI, HKUST-1, and BH-0.7-120 catalysts were quantified using a BET analyser according to a nitrogen cryosorption method and the results are summarised in Table 2. The specific surface areas of BiOI and HKUST-1 are 54.02 and 886.15 $m^2 \cdot g^{-1}$, respectively. Due to the small specific surface area of BiOI, the addition of BiOI changed the specific surface area of the composite to 120.74 $m^2 \cdot g^{-1}$, which may be due to the reduction of the specific surface area as a result of the formation of heterojunctions between the two. The adsorption–desorption isotherms and pore size distributions are shown in Figure 2d. The adsorption–desorption isotherms of the materials as-prepared all exhibit type IV with H3 hysteresis loops, indicating the mesoporous structure of the catalysts. The significantly larger specific surface area of the BH heterojunction compared to BiOI indicates that more active sites are provided for the reaction, resulting in good photocatalytic efficiency. Moreover, the narrow pore size distribution (5–30 nm) further validates the mesoporous structure.

Table 2. BET test results of different catalysts.

Catalyst	Specific Surface Area ($m^2 \cdot g^{-1}$)	Pore Volume ($cm^3 \cdot g^{-1}$)	Aperture (nm)
BiOI	54.0186	0.205676	11.9720
HKUST-1	886.1539	0.548439	6.6487
BH-0.7-120	120.7391	0.102911	6.8250

3.1.5. Photocurrent Response and Electrochemical Impedance Spectroscopy (EIS)

Photochemical tests were carried out to reveal the separation efficiency of photo-induced charge carriers for assessing the photocatalytic enhancement mechanism. The photocurrent response and electrochemical impedance spectra of BiOI, HKUST-1, and BH-0.7-120 are shown in Figure 2e,f.

As shown in Figure 2e,f, all three photocatalysts produced a photocurrent response during the same switching cycle of visible light irradiation ($\lambda \geq 400$ nm), with BiOI having the lowest photocurrent density. These results may be related to the faster compounding of its internal photogenerated electron-hole pairs. The BH-0.7-120 heterojunction has the highest photocurrent density, indicating that under visible light irradiation, BH-0.7-120 has a higher photocurrent density. The other two materials possess a higher concentration of photogenerated carriers and a better charge transfer capability.

According to the literature [28], the radius of the arc is proportional to the charge transfer resistance and inversely proportional to the photogenerated current intensity. Therefore, the smaller radius of the arc of the material reflects the lower interfacial resistance and the more efficient separation of charge carriers. As shown in Figure 2e, BH-0.7-120 exhibits the smallest radius of the arc, indicating that its formation of a heterojunction results in increased charge separation and effective suppression of electron-hole pair compounding, which are in line with the results of the photocurrent test.

3.1.6. X-ray Photoelectron Spectroscopy (XPS)

The surface elemental composition and binding energy (Bes) of the BH-0.7-120 were analysed using XPS. The full scan spectrum of BH-0.7-120 and the fine spectra of Bi, I, Cu, O, and C are shown in Figure 3.

According to the full spectrum of Figure 3f, Bi 4f5, Bi 4f7, C 1s, O 1s, I 3d3, I 3d5, Cu 2p1, and Cu 2p3 were detected at 159.19, 164.56, 284.93, 531.37, 619.57, 630.89, 933.90, and 953.11 eV, respectively, indicating the coexistence of C, O, Bi, I, and Cu elements.

In the fine spectrum of Bi in Figure 3a, there are two significant peaks at 159.52 and 164.82 eV belonging to Bi 4f7/2, and Bi 4f5/2, respectively, indicating that the predominant valence state present on the surface of BH-0.7-120 is Bi^{3+} [14]. The high-resolution spectrum of I 3d is shown in Figure 3b, where the two peaks belong to I 3d3/2 and I 3d5/2, respectively, with the peaks at 619.10 and 630.53 eV attributed to I^- and the peaks at 620.47 and 631.92 eV close to the binding energy of I^{5-} and I_2 [29]. For the O1s spectrum in Figure 3e, the peak at 529.93 eV is the Bi-O [30] in the $[Bi_2O_2]$ structure of BiOI, and the peaks at 531.19 and 532.33 eV correspond to the I-O and the O-H adsorbed on the surface, respectively. The peaks at 284.8, 286.32, and 288.69 eV in Figure 3d correspond to C-C/C-H, C-O, and O-C=O, respectively [31]. There are six peaks in the fine spectrum of Cu2p in Figure 3c; the peaks at 940.88 and 944.45 eV are satellite peaks of Cu^{2+}, the peaks at 933.59 and 953.35 eV are associated with Cu(I), and the peaks at 935.20 and 955.48 eV are associated with Cu(II), usually due to the inevitable oxidation of Cu(I) to Cu(II) [32].

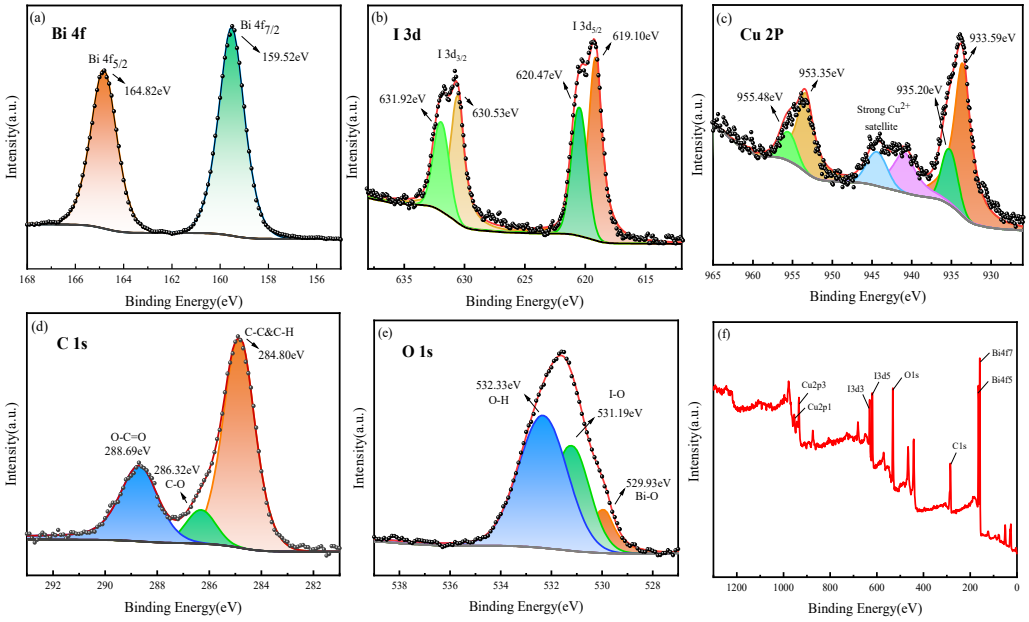

Figure 3. XPS characterisation of BH-0.7-120. (**a**) Bi 4f, (**b**) I 3d, (**c**) Cu 2P, (**d**) C 1s, (**e**) O 1s and (**f**) full spectrum of BH-0.7-120.

3.2. Photocatalytic Oxidation Performance of the BH/PMS/Light System for Degradation of AO7

The effects of six systems (BH-0.7-120, BH-0.7-120/light, BH-0.7-120/PMS, BiOI/PMS/light, HKUST-1/PMS/light, BH-0.7-120/PMS/light) on AO7 degradation were evaluated (Figure 4). Degradation experiments were carried out under visible light irradiation ($\lambda \geq 420$ nm) at initial conditions of BH-0.7-120 concentration of 0.2 g/L, PMS concentration of 0.5 mmol/L, and AO7 concentration of 200 mg/L.

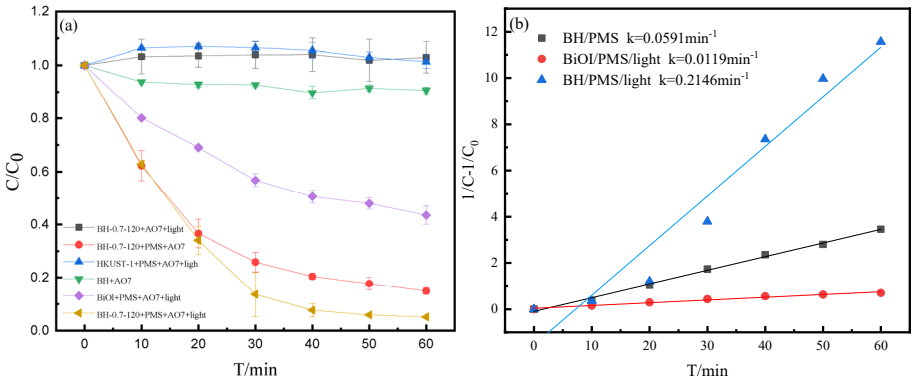

Figure 4. Effects of different systems on AO7 degradation (**a**) and kinetic fitting of degradation process (**b**). (Degradation experiments were carried out under visible light irradiation ($\lambda \geq 420$ nm) at initial conditions BH-0.7-120 concentration of 0.2 g/L, PMS concentration of 0.5 mmol/L, and AO7 concentration of 200 mg/L.)

The results showed the BH-0.7-120 photocatalyst can reach adsorption–desorption equilibrium within 30 min under dark conditions, and the adsorption rate of AO7 was only 9.4%, indicating that the adsorption efficiency of BH-0.7-120 on AO7 was weak. The degradation of AO7 by the BH-07-120/light and HKUST-1/PMS/light systems was almost zero. The possible reason was that a photocatalyst without oxidants generally degrades only low concentrations of pollutants and the HKUST-1 has a weak ability to activate PMS, so both systems did not degrade AO7 well. The AO7 degradation rates of the BiOI/PMS/light, BH-0.7-120/PMS, and BH-0.7-120/PMS/light systems were 52.5%, 85.2%, and 94.9%, respectively. The kinetic fitting for the degradation of AO7 by different systems

was performed as shown in Table 3. The degradation efficiency of AO7 by different systems conformed to the pseudo-secondary kinetic model and the degradation rate constants were 0.0119, 0.0591, and 0.2 min^{-1}, respectively. The degradation rate constants of the BH-0.7-120/PMS/light system for AO7 were 18 and 3.6 times higher than those of the other systems, respectively, indicating that the formation of heterojunctions greatly improved the photocatalytic performance of BH-0.7-120 compared with BiOI and HKUST-1.

Table 3. Degradation kinetic parameters of AO7 in BH/PMS/light system.

Catalytic System	Pseudo-First Order Kinetic			Pseudo-Second Order Kinetic		
	Rate Equation	K_{obs}/min	R^2	Rate Equation	K_{obs}/min	R^2
BH-0.7-120/PMS	$Ln(C_0/C) = 0.0315x + 0.2071$	0.0315	0.9428	$1/C - 1/C_0 = 0.0591x - 0.0933$	0.0591	0.9959
BiOI/PMS/light	$ln(C_0/C) = 0.0122x + 0.0887$	0.0122	0.9461	$1/C - 1/C_0 = 0.0119x + 0.0415$	0.0119	0.9801
BH-0.7-120/PMS/light	$ln(C_0/C) = 0.054x + 0.0692$	0.054	0.9621	$1/C - 1/C_0 = 0.2x - 0.6617$	0.2	0.9627

3.3. Effect of Different Factors on AO7 Degradation

3.3.1. Effect of Catalysts with Different Molar Ratios and Solvothermal Temperatures on AO7 Degradation

The modulation in the morphology and properties of the material by different molar ratios and different solvothermal reaction temperatures is an important factor in the preparation of good catalysts and significantly impacts the degradation properties. Figure 5a,b demonstrates the degradation rate of AO7 with time at different molar ratios and different solvothermal reaction temperatures of BiOI/HKUST-1.

Catalysts with different molar ratios have different morphology and differ in AO7 degradation performance. When the concentrations of BH, PMS, and AO7 were 0.2 g/L, 0.5 mmol/L, and 200 mg/L, respectively, the effects of different molar ratios of BH on AO7 degradation are shown in Figure 5a. All the composites showed better degradation performance than BiOI and HKUST-1 alone. With the increase in the molar ratio of BiOI/HKUST-1, the AO7 degradation rate firstly increased and then decreased. When the molar ratio rose from 0.3 to 0.7, the AO7 degradation rate increased from 77.9% to 94.9% in 60 min. When the molar ratio reached 1.0, the AO7 degradation rate decreased again to 80.4%, which had a negative impact on the photocatalytic performance. This may be due to the decline in the number of the exposed photocatalytic active sites as the specific surface area of the composite decreases. A BH molar ratio of 0.7 was chosen for the subsequent experiments.

When the concentrations of BH, PMS and AO7 were 0.2 g/L, 0.5 mmol/L, and 200 mg/L, respectively, the influence of the BH catalyst prepared at different reaction temperatures on AO7 degradation was explored (Figure 5b). The effect of different solution thermal reaction temperatures on AO7 degradation efficiency also showed an increase and then decrease with the temperature rise. The AO7 degradation rates were 63.6%, 94.9%, and 84.0% when the preparation temperature of BH was regulated to 100, 120, and 160 °C, respectively. Solvothermal reaction temperatures can regulate the chemical composition, crystallinity, and morphology of catalysts [33]. The basic features of crystal growth kinetics indicate that a too-low temperature results in slower molecular collisions and incomplete reactions, while a too-high temperature is not conducive to crystal growth. At a critical temperature, the crystalline quality is good, the morphology is regular, and the reaction is complete [34]. Therefore, BH-0.7-120 with a molar ratio of 0.7 and a solvothermal temperature of 120 °C was chosen as the best photocatalyst for subsequent experiments.

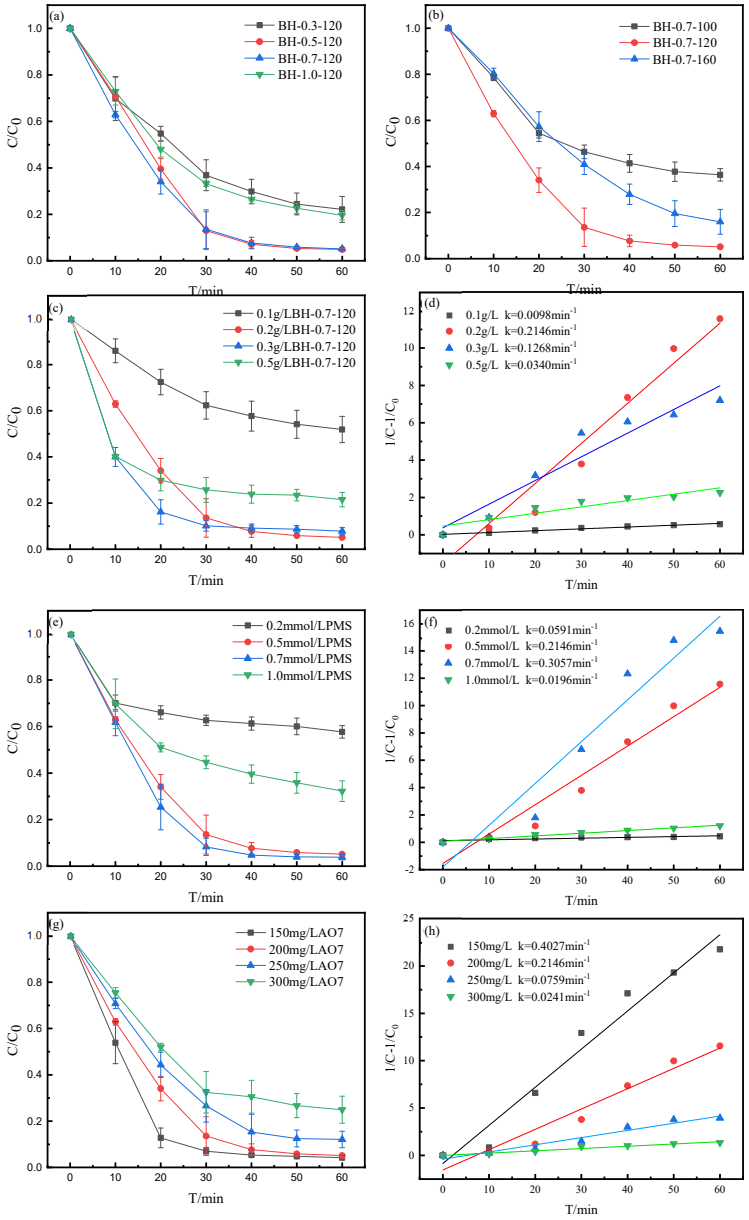

Figure 5. Effect of catalyst with different molar ratio (**a**) and solvothermal temperature (**b**) on degradation of AO7; effect of different catalyst dosages on degradation of AO7 (**c**) and kinetic fitting of degradation process (**d**); effect of different concentrations of PMS on degradation of AO7 (**e**) and kinetic fitting of degradation process (**f**); effect of different pollutant concentrations on AO7 degradation (**g**) and kinetic fitting of degradation process (**h**).

3.3.2. Effect of BH-0.7-120 Catalyst Dosing on AO7 Degradation

The catalyst dosage is a key factor affecting the degradation of AO7. The effect of the system on AO7 degradation was investigated for BH-0.7-120 catalyst dosage (0.1, 0.2, 0.3, and 0.5 g/L), PMS concentration of 0.5 mmol/L, and AO7 concentration of 200 mg/L (Figure 5c,d).

As shown in Figure 5c,d, when the amount of the BH-0.7-120 catalyst increased from 0.1 to 0.2 g/L, the AO7 degradation rate rapidly rose from 48.1% to 94.9%, and the degradation rate constant increased from 0.0098 to 0.2146 min^{-1}, which is because the increase of catalyst amount can increase the number of active sites. When the catalyst dosage continued to increase, the AO7 degradation rate gradually decreased and dropped to 75.4% at a dosage of 0.5 g/L, and the degradation rate constant decreased to 0.034 min^{-1}.

Excessive catalyst may result in high solution turbidity, which hinders light penetration and leads to light scattering and diffusion, thus reducing light utilisation and electron photogeneration, inhibiting degradation efficiency. Therefore, the optimum dosage of BH-0.7-120 is 0.2 g/L.

3.3.3. Effect of PMS Concentration on AO7 Degradation

The effect of PMS concentration (0.1, 0.5, 0.7, and 1.0 mmol/L) on the AO7 degradation rate was studied under the reaction conditions of 0.2 g/L BH-0.7-120 and 200 mg/L AO7 (Figure 5e,f).

The AO7 degradation rate first rose and then decreased with the increase of PMS dosage. When the PMS concentration increased from 0.2 to 0.5 mmol/L, the AO7 degradation rate increased from 42.3% to 94.9% and the degradation rate constant increased from 0.0591 to 0.2146 min^{-1}. An elevated level of PMS oxidant in the system produced sufficient active products for AO7 degradation. When the PMS dosage was further increased to 0.7 mmol/L, the AO7 degradation rate of 96.2% did not improve significantly due to the fact that a fixed amount of catalyst can only provide a certain number of activation sites. When the PMS concentration was further increased to 1 mmol/L, the AO7 degradation rate dropped rapidly to 67.8%. This is where the $\cdot SO_4^-$ generated from the decomposition of PMS reacts with excessive PMS to form SO_4^{2-} and therefore the degradation rate is limited. In the subsequent experiment, 0.5 mmol/L was selected as the optimum oxidant dosage.

3.3.4. Effect of Pollutant Concentration on AO7 Degradation

Figure 5g,h shows the effect of pollutant concentrations (150, 200, 250, and 300 mg/L) on AO7 degradation at a BH-0.7-120 concentration of 0.2 g/L and a PMS concentration of 0.5 mmol/L.

There is a negative linear correlation between pollutant concentration and degradation efficiency. That is, an increase in pollutant concentration decreases the AO7 degradation rate. The AO7 degradation rates were 95.7%, 94.9%, 87.9%, and 75.1% at pollutant concentrations of 150, 200, 250, and 300 mg/L, respectively, and the degradation rate constants were 0.4027, 0.2146, 0.0759, and 0.0241 min^{-1}, respectively. It was indicated that the BH-0.7-120/PMS/light system maintained good degradation rates at higher pollutant concentrations. The increased concentration of the orange–red-coloured contaminant solution impedes light transmission, while at high concentrations, there is increased competition for active sites between the intermediates and the contaminant molecules [35], both of which lead to a decrease in AO7 degradation rates. In subsequent experiments, an AO7 concentration of 200 mg/L was used.

3.4. Mechanistic Analysis

3.4.1. Free Radical Bursts

There are active substances in the process of AO7 degradation by activated persulfate in the BH-0.7-120/PMS/light system. To investigate the mechanism of AO7 degradation in the BH-0.7-120/PMS/light system, different free radical bursters were used to identify the reactive species in the reaction system. Ethanol contains α-H in its structure and has a reaction rate of 1.8–2.8 × 10^9 $M^{-1}s^{-1}$ with ·OH and 1.6–6.2 × 10^7 $M^{-1}s^{-1}$ with $\cdot SO_4^-$. Hence, ethanol has high reactivity with both ·OH and $\cdot SO_4^-$ [36] and is a good bursting agent for ·OH and $\cdot SO_4^-$. Tert-butanol has reaction rates of 3.8–7.6 × 10^8 and 4.0–9.1 × 10^5 $M^{-1}s^{-1}$ with ·OH, and $\cdot SO_4^-$, respectively, and can act as a bursting agent for ·OH [37]. As reported in recent years, during the activation of PMS, the highly reactive non-radical substance $^1O_2$ is also produced, and L-histidine can rapidly inhibit the activity of $^1O_2$ and act as a bursting agent for $^1O_2$. KI was used as a bursting agent for h^+ and also to capture $\cdot SO_4^-$ and ·OH on the catalyst surface, while p-benzoquinone was used as a bursting agent for $\cdot O_2^-$. A certain amount of a bursting agent was added at different n (bursting agent):n (PMS) ratios before the experiment, and the bursting reaction was

carried out at a catalyst concentration of 0.2 g/L, a PMS concentration of 0.5 mmol/L, and an AO7 concentration of 200 mg/L. The results are shown in Figure 6a.

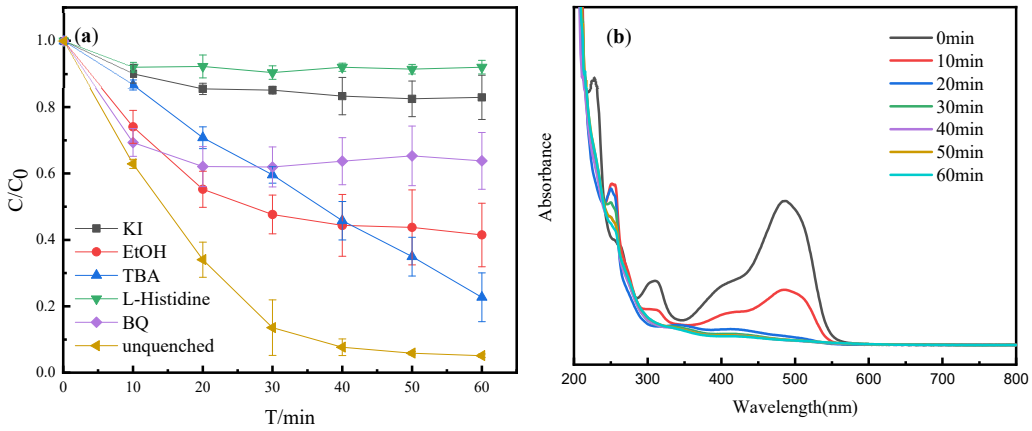

Figure 6. (**a**) Effects of different quenchers on degradation of catalytic system; (**b**) UV-Vis spectrum changes in the degradation of AO7 by BH-0.7-120/PMS/light system. (Degradation experiments were carried out under visible light irradiation ($\lambda \geq 420$ nm) at initial conditions BH-0.7-120 concentration of 0.2 g/L, PMS concentration of 0.5 mmol/L, and AO7 concentration of 200 mg/L.)

Clearly, the AO7 degradation was inhibited to some extent after the addition of the burster compared to the system without the addition of the burster. When ethanol and tert-butanol were added, the AO7 degradation was reduced to 58.5% and 77.3%, respectively, indicating that $\cdot SO_4^-$ or ·OH in the system played a role in the AO7 degradation but did not completely inhibit the reaction. It was suggested that $\cdot SO_4^-$ or ·OH was not the dominant role in the degradation process. The degradation rate was reduced to 37.5% after the addition of p-benzoquinone. The reaction was almost completely inhibited after the addition of L-histidine and the degradation rate of the system was only 9.1%. These results indicate that $\cdot O_2^-$ and $^1O_2$ in the system played an important role. The inhibition of the reaction was also obvious when KI was added to the system, indicating that the role of h^+ in the degradation system cannot be ignored, and the activation sites mainly existed on the surface of the catalyst.

3.4.2. UV-Vis Spectrogram

To study the AO7 degradation process by the BH-0.7-120/PMS/light system, the supernatant of AO7 solution after passing through a 0.45 μm filter membrane at a 10 min interval was taken and put into the UV-Vis spectrophotometer for testing in 200–800 nm. The results are shown in Figure 6b.

The molecular structure of AO7 includes a -N=N- bond, a benzene ring, and a naphthalene ring structure. As shown in Figure 6b, there are three more obvious characteristic peaks at 230, 484, and 310 nm [38], which represent the benzene ring structure, an azo structure, and a naphthalene ring structure of AO7, respectively. The characteristic peak representing -N=N- decreased rapidly within 10 min and gradually levelled off, indicating the destruction of the colour-emitting -N=N- of AO7. The intensity of the characteristic peak at 310 nm decreased with time, representing the opening of the naphthalene ring. A new characteristic peak appeared at 260 nm. The intensity of the characteristic peak was maximised at 10 min and then gradually decreased, probably resulting in new intermediates from the destruction of the structure of AO7, which then continuously decomposed into small molecules. In conclusion, the BH-0.7-120 photocatalyst has a good PMS activation effect and high degradation efficiency for AO7.

3.4.3. Degradation Mechanism Analysis

Based on the above experimental results, the AO7 degradation mechanism of the BH-0.7-120/PMS/light system was analysed (Figure 7). The binary BiOI/HKUST-1 heterojunction has the distinctive features of a type I heterojunction. At light irradiation energy above the band gap energy of the photocatalyst, both are excited to produce photogenerated electron-hole pairs (e^--h^+). According to the values of E_{VB} and E_{CB}, HKUST-1 has a higher CB potential and a lower VB potential than BiOI, so the photogenerated electrons and holes in BiOI cannot be transferred to HKUST-1 [39]. Upon excitation of BiOI and HKUST-1 by visible light energy at a certain intensity, e^- on VB leaps to CB and leaves h^+ on VB, while BiOI can also rapidly accept the free electrons generated in HKUST-1, thus accelerating the separation of electron-hole pairs. h^+ in VB of HKUST-1 migrates to VB of BiOI, and the remaining h^+ on VB of HKUST-1 and h^+ in VB of BiOI react with H_2O and OH^- in the solution to form ·OH, as shown in Equation (7). This is due to the fact that the VB potentials of both BiOI and HKUST-1 are higher than those required for ·OH formation [E(·OH/H_2O) = 1.99 eV, E(·OH/OH^-) = 2.40 eV]. The CB potential of BiOI is higher than that of the conversion of O_2 to $\cdot O_2^-$, and O_2 can be reduced to $\cdot O_2^-$, as shown in Equation (8). Meanwhile, h^+ in the VB of BiOI can directly oxidise AO7. In addition, e^- on the CB of BiOI breaks the -O-O- of perovskite to produce $\cdot SO_4^-$, thus accelerating the transfer rate of charge carriers from HKUST-1 to BiOI [25], extending the lifetime of charge carriers and reducing the complexation of electron-hole pairs. The redox potential of $\cdot SO_4^-$ is higher than that of ·OH, so $\cdot SO_4^-$ can oxidise H_2O to form ·OH, as shown in Equations (9) and (10). PMS can also autolyse slowly to produce $^1O_2$, while the resulting $\cdot O_2^-$ can react with h^+ to form H_2O_2 and $^1O_2$ [40], as shown in Equations (11) and (12). In summary, the significant improvement in the AO7 degradation efficiency of the BH-0.7-120/PMS/light system was attributed to the synergistic effect of the photocatalyst and PMS.

$$h^+ + H_2O/OH^- \rightarrow \cdot OH \quad (7)$$

$$e^- + O_2 \rightarrow \cdot O_2^- \quad (8)$$

$$e^- + HSO_5^- \rightarrow \cdot SO_4^- + OH^- \quad (9)$$

$$SO_4^- + H_2O \rightarrow H^+ + SO_4^{2-} + \cdot OH \quad (10)$$

$$HSO_5^- + SO_5^{2-} \rightarrow HSO_4^- + SO_4^{2-} + {}^1O_2 \quad (11)$$

$$2\cdot O_2^- + 2H^+ \rightarrow H_2O_2 + {}^1O_2 \quad (12)$$

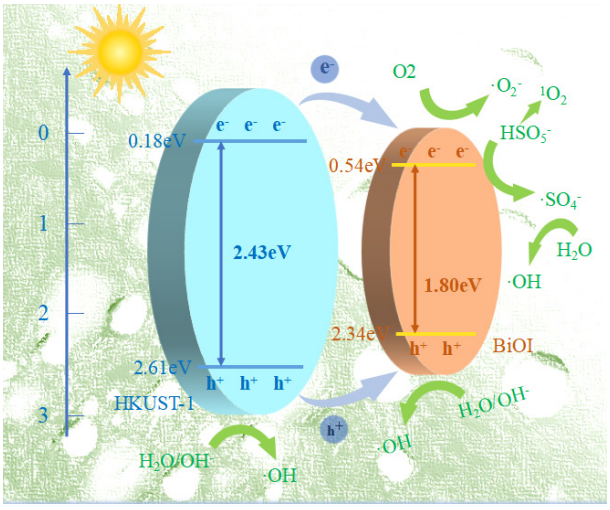

Figure 7. Degradation mechanism diagram.

4. Conclusions

A novel BiOI/HKUST-1 heterojunction was prepared from a solvothermal method. The physicochemical properties of BiOI/HKUST-1 were optimised by adjusting the solvothermal reaction temperature and molar ratio and were characterised using SEM, EDS, XRD, XPS, BET, UV-vis DRS, and electrochemical analysis. When the molar ratio increased from 0.3 to 0.7, BiOI/HKUST-1 bound completely and showed a fractured columnar structure. The best crystallisation was exhibited at a reaction temperature of 120 °C. BH-0.7-120 contains Cu, O, I, and Bi elements, with characteristic peaks for both BiOI and HKUST-1 and no other impurities, and has a forbidden band width of 2.19 eV and a specific surface area of 120.74 $m^2 \cdot g^{-1}$, exhibiting the highest photocurrent density and lowest interfacial resistance. This heterojunction was used for catalytic persulfate and the BH/PMS/light system was constructed to treat AO7 wastewater. At the catalyst, where the BH-0.7-120, PMS, and AO7 concentrations were 0.2 g/L, 0.5 mmol/L, and 200 mg/L, respectively, the reaction system can achieve an AO7 degradation efficiency of 94.9%. The five active substances, $\cdot SO_4^-$, $\cdot OH$, $\cdot O_2^-$, $^1O_2$, and h^+, in the degradation system act on the AO7 molecules to synergistically improve the AO7 degradation efficiency. The high efficiency of the combination of visible light and chemical means broadens the scope of future use in the field of water treatment, making greater use of renewable resources.

Author Contributions: Conceptualisation, X.C.; Data curation, S.Z. and R.W.; Funding acquisition, X.C.; Methodology, J.L.; Project administration, X.C.; Software, J.T.; Supervision, X.C. and J.L.; Validation, X.L.; Visualisation, J.T.; Writing—original draft preparation, S.Z. and R.W.; Writing—review and editing, X.C. All authors have read and agreed to the published version of the manuscript.

Funding: This study was supported by the National Natural Science Foundation of China (No. 51808268).

Data Availability Statement: Data are contained within the article.

Conflicts of Interest: Author Shumeng Zhang was employed by the company Hunan Research Institute for Nonferrous Metals Co., Ltd., Changsha Nonferrous Metallurgical Design and Research Institute Co., Ltd. The remaining authors declare that the research was conducted in the absence of any commercial or financial relationships that could be construed as a potential conflict of interest.

References

1. Nuengmatcha, P.; Kuyyogsuy, A.; Porrawatkul, P.; Pimsen, R.; Chanthai, S.; Nuengmatcha, P. Efficient degradation of dye pollutants in wastewater via photocatalysis using a magnetic zinc oxide/graphene/iron oxide-based catalyst. *Water Sci. Eng.* **2023**, *16*, 243–251. [CrossRef]
2. Liu, K.; Chen, J.; Sun, F.; Yu, J.; Zhang, X.; Xu, Y.; Liu, Y.; Tang, M.; Yang, Y. Enhanced degradation of azo dyes wastewater by S-scheme heterojunctions photocatalyst g-C_3N_4/MoS_2 intimately coupled *Rhodopseudomonas palustris* with chitosan modified polyurethane sponge carrier. *Int. J. Hydrogen Energy* **2023**, *48*, 22319–22333. [CrossRef]
3. Li, J.; Wang, H.; Reddy, N.; Zhu, Z.; Zheng, J.; Wang, W.; Liu, B.; Hu, C. MOFFeCo/B-CN composites achieve efficient degradation of antibiotics in a non-homogeneous concurrent photocatalytic-persulfate activation system. *Sci. Total Environ.* **2023**, *858*, 159795. [CrossRef] [PubMed]
4. Li, P.; Ma, H.; Qian, S.; Chen, Y.; Lai, B.; Pu, S. Stabilization of nFeS with carboxymethyl cellulose for enhancing persulfate activation for p-Nitrophenol degradation. *J. Environ. Chem. Eng.* **2023**, *11*, 109272. [CrossRef]
5. Che, M.; Shan, C.; Zhang, W.; Duan, Y.; Huang, R.; Cui, M.; Qi, W.; Su, R. Efficient removal of *Phaeocystis globosa* from seawater with the persulfate activation by arbutin-modified cellulose nanocrystals. *Chemosphere* **2023**, *313*, 137647. [CrossRef] [PubMed]
6. Zhou, C.S.; Cao, G.L.; Wu, X.K.; Liu, B.F.; Qi, Q.Y.; Ma, W.L. Removal of antibiotic resistant bacteria and genes by nanoscale zero-valent iron activated persulfate: Implication for the contribution of pH decrease. *J. Hazard. Mater.* **2023**, *452*, 131343. [CrossRef] [PubMed]
7. Long, X.Y.; Lei, T.; Wang, K.C.; Zhan, Z.X. Structure of Cu@Pt/C catalyst derived from HKUST-1 and its catalytic activity for methanol oxidation. *Mater. Sci. Eng. Powder Metall.* **2019**, *24*, 289–295.
8. Lin, K.S.; Adhikari, A.K.; Ku, C.N.; Chiang, C.L.; Kuo, H. Synthesis and characterization of porous HKUST-1 metal organic frameworks for hydrogen storage. *Int. J. Hydrogen Energy* **2012**, *37*, 13865–13871. [CrossRef]
9. Ma, Z.; Liu, C.; Srinivasakannan, C.; Li, L.; Wang, Y. Synthesis of magnetic Fe_3O_4-HKUST-1 nanocomposites for azo dye adsorption. *Arab. J. Chem.* **2023**, *16*, 104767. [CrossRef]
10. Wang, W.; Ji, Z.; Zhang, D.; Sun, P.; Duan, J. TiO_2 doped HKUST-1/CM film in the three-phase photocatalytic ammonia synthesis system. *Ceram. Int.* **2021**, *47*, 19180–19190. [CrossRef]

11. Jalali, S.; Rahimi, M.R.; Dashtian, K.; Ghaedi, M.; Mosleh, S. One step integration of plasmonic Ag_2CrO_4/Ag/AgCl into HKUST-1-MOF as novel visible-light driven photocatalyst for highly efficient degradation of mixture dyes pollutants: Its photocatalytic mechanism and modeling. *Polyhedron* **2019**, *166*, 217–225. [CrossRef]
12. Wang, Z.; Ma, Y.; Shi, Y.; Wang, S.; Gao, M.; Qiu, Y.; Li, C. Bi_2WO_6/red phosphorus heterojunction photocatalyst with excellent visible light photodegrading activity. *Chem. Phys. Lett.* **2023**, *818*, 140422. [CrossRef]
13. Sheikhsamany, R.; Faghihian, H.; Fazaeli, R. One-pot synthesis of $BaTi_{0.85}Zr_{0.15}O_3$/MOF-199 (HKUST-1) as a highly efficient photocatalytic nanocomposite for tetracycline degradation under UV irradiation. *Inorg. Chem. Commun.* **2021**, *134*, 109048. [CrossRef]
14. Wu, D.; Tian, N.; Sun, X.; Wang, M.; Huang, J.; Deng, H.; Yu, D.; Wu, M.; Ni, H.; Pei, K.; et al. Enhanced fenton-like catalysis by facilely prepared nano-scale NCFOH/HKUST composites with synergistic effect for dye degradation. *Mater. Chem. Phys.* **2021**, *258*, 123980. [CrossRef]
15. Haile, C.T.; Ahmad, N.; Chiu, C.-W.; Kuo, C.-F.J. Highly photoactive novel NiS/BiOI nanocomposite photocatalyst towards efficient visible light organic pollutant degradation and carcinogenetic Cr (VI) reduction for environmental remediation. *Chemosphere* **2023**, *323*, 138108. [CrossRef] [PubMed]
16. Xu, H.Y.; Wang, W.S.; Li, B.; Zhang, L. Mechanism insights into the enhanced photocatatlytic peroxydisulfate activation by Fe_3O_4/BiOI heterojunction. *Mater. Sci. Eng. B* **2023**, *294*, 116509. [CrossRef]
17. Xiong, J.; Zhu, X.; Xia, J.; Di, J. Partial disorder structured BiOI atomic layers boosting excitons dissociation for photocatalytic CO_2 reduction and pollutant removal. *Appl. Surf. Sci.* **2023**, *627*, 157338. [CrossRef]
18. Zhang, J.J.; Zheng, Y.J.; Jing, T.; Zhao, Y.; Yang, W. 3D flower-shaped MoS_2/O-g-C_3N_4 Z-type heterojunction enhances the photocatalyst degradation of bisphenol A. *Acta Mater. Compos. Sin.* **2022**, *39*, 5778–5791.
19. Pan, J.; Bai, X.; Li, Y.; Yang, B.; Yang, P.; Yu, F.; Ma, J. HKUST-1 derived carbon adsorbents for tetracycline removal with excellent adsorption performance. *Environ. Res.* **2022**, *205*, 112425. [CrossRef]
20. Zhang, H.; Xiao, Y.; Peng, Y.; Tian, L.; Wang, Y.; Tang, Y.; Cao, Y.; Wei, Z.; Wu, Z.; Zhu, Y.; et al. Selective degradation of ceftriaxone sodium by surface molecularly imprinted BiOCl/Bi_3NbO_7 heterojunction photocatalyst. *Sep. Purif. Technol.* **2023**, *315*, 123716. [CrossRef]
21. Ma, H.; Wang, Y.; Zhang, Z.; Liu, J.; Yu, Y.; Zuo, S.; Li, B. A superior ternary Z-scheme photocatalyst of bi/black phosphorus nanosheets/P-doped BiOCl containing interfacial P–P bond and metallic mediator for H_2O_2 production and RhB degradation. *Chemosphere* **2023**, *330*, 138717. [CrossRef] [PubMed]
22. Yuan, L.; Wang, Z.; Gu, F. Efficient degradation of tetracycline hydrochloride by direct Z-scheme HKUST-1@ m-$BiVO_4$ catalysts with self-produced H_2O_2 under both dark and light. *J. Environ. Chem. Eng.* **2022**, *10*, 107964. [CrossRef]
23. Wu, Y.; Li, Y.; Li, H.; Guo, H.; Yang, Q.; Li, X. Tunning heterostructures interface of Cu_2O@HKUST-1 for enhanced photocatalytic degradation of tetracycline hydrochloride. *Sep. Purif. Technol.* **2022**, *303*, 122106. [CrossRef]
24. Sheikhsamany, R.; Faghihian, H.; Fazaeli, R. Synthesis of novel HKUST-1-based SnO_2 porous nanocomposite with the photocatalytic capability for degradation of metronidazole. *Mater. Sci. Semicond. Process.* **2022**, *138*, 106310. [CrossRef]
25. Li, Y.; Wang, X.; Huo, H.; Li, Z.; Shi, J. A novel binary visible-light-driven photocatalyst type-I $CdIn_2S_4$/g-C_3N_4 heterojunctions coupling with H_2O_2: Synthesis, characterization, photocatalytic activity for Reactive Blue 19 degradation and mechanism analysis. *Colloids Surf. A Physicochem. Eng. Asp.* **2020**, *587*, 124322. [CrossRef]
26. Liu, S.Q.; Dai, G.P.; Liang, Y.; Liu, H.; Zhang, X. Preparation of BiOI/Bi_2O_3 Photocatalyst with Highly Visible-Light Photocatalytic Activity by an In Situ Dissolving-Depositing Method. *Chin. J. Inorg. Chem.* **2011**, *27*, 1964–1968.
27. Sofi, F.A.; Majid, K.; Mehraj, O. The visible light driven copper based metal-organic-framework heterojunction: HKUST-1@ Ag-Ag_3PO_4 for plasmon enhanced visible light photocatalysis. *J. Alloys Compd.* **2018**, *737*, 798–808. [CrossRef]
28. Zhao, B.; Shao, N.; Chen, X.; Ma, J.; Gao, Y.; Chen, X. Construction of novel type II heterojunction WO_3/Bi_2WO_6 and Z-scheme heterojunction CdS/Bi_2WO_6 photocatalysts with significantly enhanced photocatalytic activity for the degradation of rhodamine B and re-duction of Cr (VI). *Colloids Surf. A Physicochem. Eng. Asp.* **2023**, *663*, 131072. [CrossRef]
29. Qin, H.; Lv, Y.; Kobayashi, H.; Xiao, M.; Song, H.; Yang, J. Fabrication of NOTT-220 @I2 via iodine adsorption and immobilization in bismuth organic framework for efficient CO_2 photo-reduction. *J. Alloys Compd.* **2022**, *920*, 165900. [CrossRef]
30. Xu, W.; Fang, J.; Zhu, X.; Fang, Z.; Cen, C. Fabricaion of improved novel p–n junction BiOI/$Bi_2Sn_2O_7$ nanocomposite for visible light driven photocatalysis. *Mater. Res. Bull.* **2015**, *72*, 229–234. [CrossRef]
31. Li, J.; Yu, X.; Zhu, Y.; Fu, X.; Zhang, Y. 3D-2D-3D BiOI/porous g-C_3N_4/graphene hydrogel composite photocatalyst with synergy of adsorption-photocatalysis in static and flow systems. *J. Alloys Compd.* **2021**, *850*, 156778. [CrossRef]
32. Wu, Y.; Li, X.; Zhao, H.; Yao, F.; Cao, J.; Chen, Z.; Wang, D.; Yang, Q. Core-shell structured Cu_2O@HKUST-1 heterojunction photocatalyst with robust stability for highly efficient tetracycline hydrochloride degradation under visible light. *Chem. Eng. J.* **2021**, *426*, 131255. [CrossRef]
33. Nunes, M.J.; Lopes, A.; Pacheco, M.J.; Ciríaco, L. Visible-Light-Driven AO7 Photocatalytic Degradation and Toxicity Removal at Bi-Doped $SrTiO_3$. *Materials* **2022**, *15*, 2465. [CrossRef] [PubMed]
34. Qi, X.M.; Wu, J.; Wu, Q.; Li, X.; Gu, M.L. Research Progress on Controllable Synthesis Multiple Morphologies and Structures of $BiVO_4$ via Hydrothermal/Solvothermal Method. *Mater. Rev.* **2014**, *28*, 74–78.

35. Ntelane, T.S.; Feleni, U.; Mthombeni, N.H.; Kuvarega, A.T. Heterogeneous activation of persulfate using delafossite $AgFeO_2$/α-MnO_2 for efficient degradation of tartrazine under visible light. *Colloids Surf. A Physicochem. Eng. Asp.* **2023**, *670*, 131492. [CrossRef]
36. Tang, Q.; An, X.; Zhou, J.; Lan, H.; Liu, H.; Qu, J. One-step exfoliation of polymeric C_3N_4 by atmospheric oxygen doping for photocatalytic persulfate activation. *J. Colloid Interface Sci.* **2020**, *579*, 455–462. [CrossRef]
37. Lin, L.; Yu, D.; Xu, L.; Huang, Y.; Huang, M.; Kazemian, H. Enhanced photocatalytic performance and persulfate activation properties by BiOBr supported waste rock wool fibers under LED blue light. *J. Environ. Chem. Eng.* **2022**, *10*, 107963. [CrossRef]
38. Wang, Y.; Wei, C.Y.; Huang, T.Y.; Wu, W.; Chen, J.B. Activation of peroxymonosulfate by nitrogen-doped carbon nanotubes to decolorize acid orange 7. *China Environ. Sci.* **2017**, *37*, 2583–2590.
39. Zhu, K.; Zhang, F.; Cai, W.; Liu, C.; Wang, Y.; Meng, Z.; Mi, C. A novel I-type 0D/0D $ZnS/Ag_6Si_2O_7$ heterojunction for photocatalytic hydrogen evolution. *J. Phys. Chem. Solids* **2023**, *175*, 111206. [CrossRef]
40. Wang, Q.; Mei, Y.; Zhou, R.; Komarneni, S.; Ma, J. Persulfate activation of CuS@Ti_3C_2-based MXene with Bi-active centers toward Orange II removal under visible light. *Colloids Surf. A Physicochem. Eng. Asp.* **2022**, *648*, 129315. [CrossRef]